Full electromagnetic Vlasov code simulation of the Kelvin–Helmholtz instability

Takayuki Umeda,[1,a)] Jun-ichiro Miwa,[1] Yosuke Matsumoto,[1] Takuma K. M. Nakamura,[2] Kentaro Togano,[1] Keiichiro Fukazawa,[3] and Iku Shinohara[2]
[1]*Solar-Terrestrial Environment Laboratory, Nagoya University, Nagoya 464-8601, Japan*
[2]*Institute of Space and Astronautical Science, Japan Aerospace Exploration Agency, Sagamihara 229-8510, Japan*
[3]*Department of Earth and Planetary Sciences, Kyushu University, Fukuoka 812-8581, Japan*

(Received 11 December 2009; accepted 12 April 2010; published online 18 May 2010)

Recent advancement in numerical techniques for Vlasov simulations and their application to cross-scale coupling in the plasma universe are discussed. Magnetohydrodynamic (MHD) simulations are now widely used for numerical modeling of global and macroscopic phenomena. In the framework of the MHD approximation, however, diffusion coefficients such as resistivity and adiabatic index are given from empirical models. Thus there are recent attempts to understand first-principle kinetic processes in macroscopic phenomena, such as magnetic reconnection and the Kelvin–Helmholtz (KH) instability via full kinetic particle-in-cell and Vlasov codes. In the present study, a benchmark test for a new four-dimensional full electromagnetic Vlasov code is performed. First, the computational speed of the Vlasov code is measured and a linear performance scaling is obtained on a massively parallel supercomputer with more than 12 000 cores. Second, a first-principle Vlasov simulation of the KH instability is performed in order to evaluate current status of numerical techniques for Vlasov simulations. The KH instability is usually adopted as a benchmark test problem for guiding-center Vlasov codes, in which a cyclotron motion of charged particles is neglected. There is not any full electromagnetic Vlasov simulation of the KH instability; this is because it is difficult to follow $\vec{E}\times\vec{B}$ drift motion accurately without approximations. The present first-principle Vlasov simulation has successfully represented the formation of KH vortices and its secondary instability. These results suggest that Vlasov code simulations would be a powerful approach for studies of cross-scale coupling on future Peta-scale supercomputers.
 [doi:10.1063/1.3422547]

I. INTRODUCTION

Space plasma is collisionless, multiscale, and highly nonlinear media. Thus computer simulations are essential approaches for studies of space plasma. There are numerous types of self-consistent computer simulations that treat plasmas according to some approximation. The macroscopic (global-scale) dynamics in space plasma are commonly described by magnetohydrodynamic (MHD) and Hall-MHD models. On the other hand, microscopic (electron-scale) processes in space plasma are described by the full kinetic models, i.e., Maxwell's equations and either the Newton–Lorentz equation for charged particles or the Vlasov (collisionless Boltzmann) equation. Hybrid methods whereby treat ions as particles and electrons as a fluid for mesoscopic (ion-scale) processes.

In recent days, the MHD simulations are widely used for numerical modeling of the solar wind, solar flares, global planetary magnetospheres, and other macroscopic phenomena. However, the MHD simulations need resistivity, conductivity, adiabatic index, and diffusion coefficients. These quantities are essentially due to first-principle kinetic processes that are eliminated in the framework of the conventional MHD approximation. Recent high-resolution *in situ* observations have also suggested that the macroscopic, mesoscopic, and microscopic processes in space plasma are strongly coupled with each other, which is called cross-scale coupling. To go toward the cross-scale coupling in the plasma universe, it is important to include full kinetics of plasma particles in global and macroscale simulations. However, this requires an enormous computing resource.

There are recent attempts to directly simulate macroscale processes, such as magnetic reconnection and the Kelvin–Helmholtz (KH) instability via full kinetic codes. The full electromagnetic particle-in-cell (PIC) code, in which both electrons and ions are treated as individual charged particles, is very powerful for describing the full kinetics in space plasma. Especially, the standard explicit PIC method is a well-developed numerical technique, which has large benefits that numerical procedures and concepts are quite simple without approximation in the basic laws of collisionless plasmas. However, this method has two severe restrictions. First, a limitation on the number of particles in the PIC method gives rise to strong numerical thermal fluctuations. Second, one needs to set the grid spacing Δ to be as short as the electron Debye length, which makes it difficult to perform large PIC simulations of MHD-scale processes on limited computer resources. Note that the implicit PIC methods can relax the constraint (e.g., Ref. 1). A fully implicit time step-

a)Electronic mail: umeda@stelab.nagoya-u.ac.jp.

ping PIC method was used for studies of magnetic reconnection.[2] However, the fully implicit methods need modification of the basic equations, and their numerical procedures are much more complicated than those of the explicit PIC method.

The Vlasov method, which follows spatial and temporal developments of distribution functions defined in the position-velocity phase space, is considered to be an alternative to the PIC method because the Vlasov method is free from any numerical noise. On the other hand, one needs a huge number of grid points in both configuration and velocity spaces to treat six-dimensional phase space, which is a big drawback of the current Vlasov method. In recent days, however, numerical techniques for Vlasov simulations are rapidly developing as well as the rapid development of hardware technology. Very recently, there are several successful benchmark tests of geospace environment modeling of magnetic reconnection[3] via Darwin-approximated or full electromagnetic Vlasov codes.[4,5] It has been demonstrated that the Vlasov method can relax the constraint of grid spacing. That is, one can set the grid spacing Δ to be much longer than the electron Debye length.[5]

Roles of the first-principle kinetic model, i.e., PIC or Vlasov method, would be more essential in future space plasma simulations. We regard the Vlasov method as a potential candidate for simulations of cross-scale coupling in the plasma universe. In this paper, the current status of the Vlasov method is studied by performing benchmark tests of the KH instability.

The KH instability is a macroscopic process in which MHD-scale vortices are generated. The shear plasma flow, which drives the KH instability, corresponds to the plasma convection, i.e., the motion of both plasma particles and magnetic fields. Since the plasma convection results from the $\vec{E}\times\vec{B}$ drift of plasma particles, it is essential to solve the $\vec{E}\times\vec{B}$ drift as accurate as possible in kinetic simulations. It is also well known that smaller-scale vortices are also generated in the MHD-scale vortices (e.g., Refs. 6 and 7). The cross-scale coupling between large- and smaller-scale vortices in the KH instability can be induced by secondary instabilities, such as the Rayleigh–Taylor (RT) instability, current sheet kink instability, and magnetic reconnection (e.g., Refs. 6 and 8). From a view point of the cross-scale coupling between fluid processes and kinetic processes, MHD-scale vortices can be diffused by the cyclotron motion of ion particles. However, it is not easy to include full kinetics in the MHD-scale process via full particle simulations due to several numerical difficulties. Thus we benchmark a new full electromagnetic Vlasov code by the KH instability with a simple geometry, in which a uniform out-of-plain magnetic field exists without in-plain magnetic fields. This geometry allows us to reduce one (out-of-plain) velocity dimension. That is, we can save computing resources substantially by taking the simulation domain in a four-dimensional (4D) phase space with two spatial dimensions and two (in-plain) velocity dimensions.

This paper is structured as follows. In Sec. II, numerical techniques for the full electromagnetic Vlasov code are briefly reviewed. In Sec. III, computational performance of our 4D Vlasov code is measured on a scalar massively parallel computer. In Sec. IV, simulation setup for the KH instability and numerical results are presented. The summary is given in Sec. V.

II. BRIEF REVIEW OF VLASOV CODE

The Vlasov method solves the full set of Maxwell's equations (1) and the Vlasov equation (2),

$$\left.\begin{aligned}\nabla\times\vec{B}&=\mu_0\vec{J}+\frac{1}{c^2}\frac{\partial\vec{E}}{\partial t}\\ \nabla\times\vec{E}&=-\frac{\partial\vec{B}}{\partial t}\\ \nabla\cdot\vec{E}&=\frac{\rho}{\epsilon_0}\\ \nabla\cdot\vec{B}&=0\end{aligned}\right\} \tag{1}$$

$$\frac{\partial f_s}{\partial t}+\vec{v}\frac{\partial f_s}{\partial\vec{x}}+\frac{q_s}{m_s}[\vec{E}+\vec{v}\times\vec{B}]\frac{\partial f_s}{\partial\vec{v}}=0, \tag{2}$$

where $\vec{E}$, $\vec{B}$, $\vec{J}$, ρ, μ_0, ϵ_0, and c represent electric field, magnetic field, current density, charge density, magnetic permeability, dielectric constant, and light speed, respectively. The distribution functions $f_s(\vec{x},\vec{v},t)$ are defined in a position-velocity phase space. The subscript s represents the singly charged ions and electrons (e.g., $s=i,e$). The quantities q_s and m_s are the charge and mass of particle species s. The current density $\vec{J}$ is determined so that ρ and $\vec{J}$ satisfy the current-continuity equation

$$\frac{\partial\rho}{\partial t}+\nabla\cdot\vec{J}=0. \tag{3}$$

The Vlasov equation (2) consists of advection equations with a constant advection velocity and a rotation equation by a centripetal force without diffusion terms. It is not so easy to integrate the Vlasov equation numerically without artificial viscosity. Thus the operator splitting technique (e.g., Refs. 9 and 10) is applied to simplify the numerical integration of the Vlasov equation. Then, the Vlasov equation splits into the following three equations:

$$\frac{\partial f_s}{\partial t}+\vec{v}\frac{\partial f_s}{\partial\vec{x}}=0, \tag{4}$$

$$\frac{\partial f_s}{\partial t}+\frac{q_s}{m_s}\vec{E}\frac{\partial f_s}{\partial\vec{v}}=0, \tag{5}$$

$$\frac{\partial f_s}{\partial t}+\frac{q_s}{m_s}[\vec{v}\times\vec{B}]\frac{\partial f_s}{\partial\vec{v}}=0. \tag{6}$$

Equations (4) and (5) are scalar (linear) advection equations in which $\vec{v}$ and $\vec{E}$ are independent of $\vec{x}$ and $\vec{v}$, respectively. Thus a multidimensional conservative semi-Lagrangian scheme[5] is straightforwardly applied (see Appendix for more detail),

$$f_s^{t+\Delta t} \leftarrow f_s^t + \nabla \cdot \vec{U}_s \Delta t. \tag{7}$$

It should be noted that it is essential for satisfying the current-continuity equation to use conservative schemes (e.g., Refs. 11–13) for solving the advection equation in configuration space (4).

Equation (6), on the other hand, is a multidimensional rotation equation that follows a circular motion of a profile at constant speed by a centripetal force. For stable rotation of the profile on the Cartesian grid system, the "backsubstitution" technique[14] is applied. In addition, Maxwell's equations are solved by the implicit finite difference time domain (FDTD) method on the Yee grid system,[15] which is free from the Courant–Friedrichs–Lewy (CFL) condition for electromagnetic light mode waves.[16]

In this paper, we use a modified version of the splitting scheme (e.g., Ref. 17), which is consistent with the second-order leap-frog time-integration algorithm used in PIC simulations. It is noted that we use a positive, conservative, and nonoscillatory scheme[13] for shifting of distribution functions via numerical interpolation. The Maxwell–Vlasov system is advanced by using the following sequences.

(1) Shift phase-space distribution functions in the configuration space with the full time step Δt by using the multidimensional conservative scheme,[5]

$$f_s^*(\vec{x},\vec{v}) \leftarrow f_s^t(\vec{x} - \vec{v}\Delta t, \vec{v}). \tag{8}$$

(2) Compute the current density by integrating numerical flux in Eq. (7) over the velocity $\vec{v}$,

$$\vec{J}^{t+(\Delta t/2)} = \sum_s q_s \int \vec{U}_s \mathrm{d}\vec{v}. \tag{9}$$

(3) Advance electromagnetic fields from t to $t+\Delta t$ by solving Maxwell's equations with the implicit FDTD method.

(4) Shift phase-space distribution functions in the velocity space by an electric force with the half time step $\Delta t/2$ by using the multidimensional conservative scheme,[5]

$$f_s^{**}(\vec{x},\vec{v}) \leftarrow f_s^*\left(\vec{x},\vec{v} - \frac{q_s}{m_s}\vec{E}^{t+\Delta t}\Delta t\right). \tag{10}$$

(5) Rotate phase-space distribution functions in the velocity space by a magnetic force with the full time step Δt by using the backsubstitution scheme,[14]

$$f_s^{***}(\vec{x},\vec{v}) \leftarrow f_s^{**}(\vec{x},\vec{v}^*), \tag{11}$$

where

$$\vec{v}^* = \vec{v} - \frac{q_s}{m_s}\frac{\Delta t}{1+\left[\frac{q_s}{m_s}\frac{\Delta t}{2}|\vec{B}^{t+\Delta t}|\right]^2}[\vec{v}\times\vec{B}^{t+\Delta t}] + \frac{q_s^2}{2m_s^2}\frac{\Delta t^2}{1+\left[\frac{q_s}{m_s}\frac{\Delta t}{2}|\vec{B}^{t+\Delta t}|\right]^2}[\vec{v}\times\vec{B}^{t+\Delta t}\times\vec{B}^{t+\Delta t}].$$

(6) Shift phase-space distribution functions in the velocity space by an electric force with the half time step $\Delta t/2$ by using the multidimensional conservative scheme,[5]

$$f_s^{t+\Delta t}(\vec{x},\vec{v}) \leftarrow f_s^{***}\left(\vec{x},\vec{v} - \frac{q_s}{m_s}\vec{E}^{t+\Delta t}\Delta t\right). \tag{12}$$

As demonstrated by Umeda *et al.*,[5] a numerical constraint on the spatial grid can be relaxed in the full electromagnetic Vlasov simulation. That is, the grid spacing can be taken to be much longer than the electron Debye length, if the Debye-scale physics can be negligible. It should be noted, however, that low resolutions in configuration or velocity spaces sometimes cause numerical diffusion of physical structures, as we show in the present study.

In the present Vlasov code, we have three numerical constraints on the time step. The first is the CFL condition for advection in configuration space,

$$\frac{1}{\sqrt{1/\Delta x^2 + 1/\Delta y^2}} > |\boldsymbol{v}_{\max}|\Delta t, \tag{13}$$

which might not be important. The second is the CFL condition for advection in velocity space by electric fields,

$$\frac{1}{\sqrt{1/\Delta v_x^2 + 1/\Delta v_y^2}} > \frac{q}{m}|\boldsymbol{E}|\Delta t. \tag{14}$$

This becomes critical when a strong electric field arises. The third is the CFL condition for rotation in velocity space by magnetic fields,

$$\frac{1}{\sqrt{1/\Delta v_x^2 + 1/\Delta v_y^2}} > \frac{q}{m}|\boldsymbol{v}_{\max}||\boldsymbol{B}|\Delta t, \tag{15}$$

which is most important in the present study. For stable rotation of distribution functions with the backsubstitution scheme on the Cartesian grid system, we choose the time step Δt such that

$$\Delta v_e > \frac{q_e}{m_e}|\boldsymbol{v}_{\max,e}|B_0\Delta t = \omega_{ce}|\boldsymbol{v}_{\max,e}|\Delta t. \tag{16}$$

III. WEAK SCALING PERFORMANCE ON MASSIVELY PARALLEL COMPUTERS

There is some additional communication overhead in parallelizing over the velocity dimensions since a reduction operation is required to calculate current and charge densities at a given point in configuration space. Thus the present 4D Eulerian Vlasov code is parallelized via domain decomposition only in configuration space. The distribution functions and electromagnetic fields are domain decomposed over the two spatial dimensions, which involves the exchange of ghost values for f, E_x, E_y, and B_z along each processing element (PE) boundary. A simulation domain of size $(N_x, N_y, N_{v_x}, N_{v_y})$ is decomposed onto n_{pe} PEs, where $n_{pe}=n_{pex}\times n_{pey}$, in local domains of size $(N_x/n_{pex}, N_y/n_{pey}, N_{v_x}, N_{v_y})$. Communication between PEs is carried out by using the "mpi_sendrecv" subroutine in the standard message passing interface library for simplicity and portability.

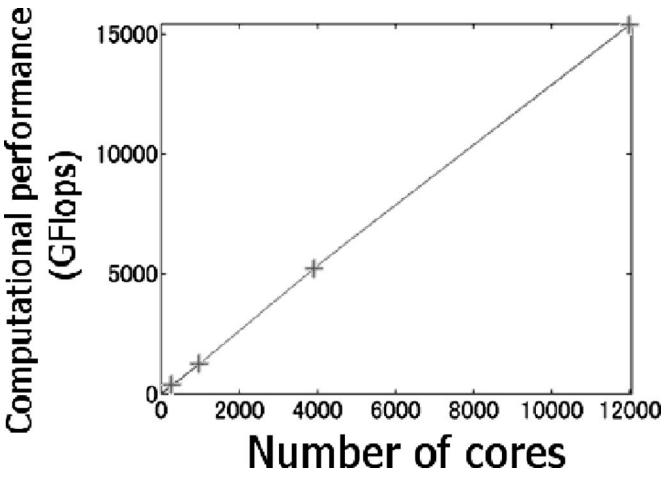

FIG. 1. Computational performance of the 4D Vlasov code as a function of the number of processor cores measured on the Fujitsu FX1 system.

We start the performance measurement test with a phase-space grid of $(N_x,N_y,N_{v_x},N_{v_y})=(80,40,80,80)$ on one PE. That is, a weak-scaling test is conducted by fixing a "computational" load on one PE. The tests were completed on Fujitsu FX1 systems (1CPU/node) at Information Technology Center in Nagoya University (256 nodes) and JAXA's Engineering Digital Innovation (JEDI) center (3008 nodes) based on 2.5 GHz quad-core SPARC64 VII processors. As the number of PEs is quadrupled, the number of total grids is doubled in both x and y directions with the constant size of local domains.

Figure 1 shows the computational performance as a function of the number of processor cores. The computational performance is measured by the hardware counter installed on the Fujitsu FX1 systems. As the peak performance with 1 core, 256 cores (=4 cores$\times$64 node), 1024 cores (=4 cores$\times$256 node), and 12 032 cores (=4 cores $\times$3008 node), we achieved 1.38GFlops, 335.4GFlops, 1.35TFlops, and 15.4TFlops, respectively. The computational performance scales almost linearly as the number of processor cores increases. The parallel efficiency is over 90% with 12 032 cores.

In general, it is not easy to parallelize PIC codes. This is because the PIC method has both Eulerian variables (electromagnetic fields) and Lagrangian variables (particle positions and velocities), and we need to decompose both particles and fields onto PEs. The particle decomposition method is sometimes used when the computational domain is not so large, in which only particle data are decomposed onto PEs and each PE has all field data. One can easily find that the computational domain cannot be extended with the particle decomposition method because of the memory limit. The domain decomposition method is an alternative approach, in which the computational domain is directly decomposed onto PEs. Thus particles are also decomposed onto each PE. An issue arises when the number of particles on each PE becomes nonuniform. The computational load on each PE also becomes nonuniform. Hence, special load balancing algorithms (e.g., Ref. 18) are needed. In PIC simulations of the KH instability, the number of particles in a local computational domain dynamically varies. We need additional overhead processing and communications for load balancing between PEs. Hence it becomes difficult to obtain an ideal scalability in PIC simulations. The present weak-scaling test suggests that it is easier to obtain an ideal scalability in Vlasov simulations than PIC simulations. This is because the Vlasov method has only Eulerian variables and it is easy to decompose the computational domain equally.

IV. THE KELVIN–HELMHOLTZ INSTABILITY

Convection of plasma (i.e., motion of both plasma particles and magnetic fields) is essential for describing global- and macroscale processes. Since the plasma convection corresponds to the $\vec{E}\times\vec{B}$ drift in the plasma kinetics, it is important to solve the $\vec{E}\times\vec{B}$ as accurate as possible. The KH instability is a good example as a benchmark test problem for Vlasov codes because the instability is driven by a velocity shear between two convecting plasma flows. Note that the KH instability has been chosen as a benchmark test problem for a "guiding-center" Vlasov method (e.g., Ref. 19), in which velocities across the ambient magnetic field are approximated by the drift velocity $\vec{v}_D\equiv\vec{E}\times\vec{B}/B^2$ and the cyclotron motion of charged particles are neglected. Thus it is not clear whether previous Vlasov codes can follow the $\vec{E}\times\vec{B}$ drift accurately. The present study is the first attempt for benchmark testing of the full electromagnetic Vlasov method by using the KH instability.

A. Simulation setup

We assume two-dimensional (2D) simulation domain taken in the x-y plain. The velocity space is also assumed to be in the v_x-v_y plain. Thus the Vlasov equation is solved in the 4D phase space. In this model, in-plain magnetic fields, out-of-plain motions, currents, and electric fields are neglected. We use $N_x\times N_y=128\times160$ grid cells. We change the number of grid cells for velocity space as $N_{v_x}\times N_{v_y}=80\times80$ (run A), 60×60 (run B), and 40×40 (run C).

We adopt the initial condition used by Matsumoto and Hoshino[6] in order to make a direct comparison between Vlasov and PIC simulations. The initial condition is maintained by the MHD equilibrium with the unperturbed velocity directed in the x direction and sheared in the y direction. A uniform (background) magnetic field is applied in the z direction, and thus the plasma thermal pressure is uniformly set in the simulation domain. The number density is provided as a function of y,

$$n_s(y)=\frac{n_0}{2}\{(1+\alpha)+(1-\alpha)\tanh(y/l)\}, \tag{17}$$

$$u_{x,s}(y)=-\frac{u_0}{2}\tanh(y/l), \tag{18}$$

where l and α represent the "half thickness" of the shear layer and the asymptotic number density ratio relative to the value of $n[+\infty]$, respectively. The subscript $s=e$ and i represents particle species (electron and ion). The number density at $y=-\infty$ corresponds to $n_0=\epsilon_0 m_i\omega_{pi}^2/q_i^2$ with ϵ_0, m, q, and ω_p

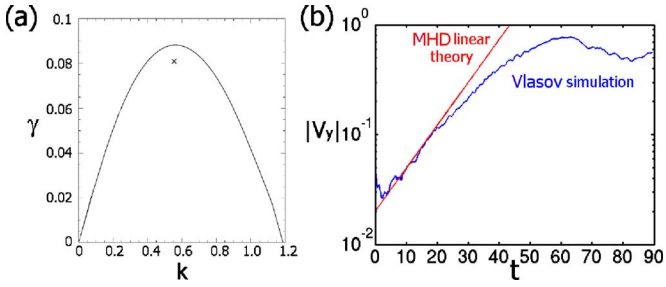

FIG. 2. (Color online) (a) Growth rate as a function of the wavenumber in the flow direction obtained by linear analysis of the ideal MHD equations. The growth rate and wavenumber is normalized by l/u_0 and $1/l$, respectively. The x mark represents the growth rate of the most unstable KH vortex obtained by the Vlasov simulation. (b) Time development of the most unstable KH vortex. The ordinate shows the power of the y component of the perturbed ion velocity at the most unstable wavenumber ($k_x \sim 0.56$), obtained by the Fourier transformation. The velocity is normalized by the initial velocity jump (u_0), and the time is normalized by u_0/l. As a reference, the growth rate obtained by the linear analysis of the ideal MHD equations is also shown.

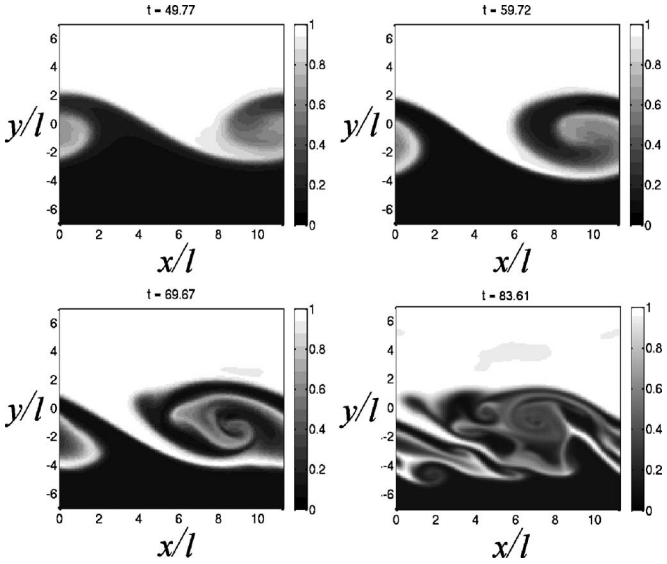

FIG. 3. Spatial profiles of the ion number density at different times in run A. The time is normalized by l/u_0.

being the vacuum permittivity, mass, charge, and plasma frequency (at $y=-\infty$), respectively. The half thickness of the shear layer is chosen to be $l=8.0r_i$ ($r_i=v_{ti}/\omega_{ci}$), where r, v_t, and ω_c are the thermal cyclotron radius, thermal velocity (at $y=+\infty$), and cyclotron frequency. The velocity shear is chosen to be $u_0=\sqrt{V_A^2+V_S^2}=7.28v_{ti}$, with the Alfven velocity $V_A=7.0v_{ti}$ and the ion sound velocity $V_S=2.0v_{ti}$. The ion cyclotron frequency is set as $\omega_{ci}/\omega_{pi}=0.0875$, and the speed of light is set as $c/v_{ti}=80.0$. For computational efficiency we adopt a very small number of the ion-to-electron mass ratio, $m_i/m_e=16$. The ion-to-electron temperature ratio is chosen to be $T_i/T_e=1$.

A number density ratio of $\alpha=0.1$ is chosen in the present study. Thus the plasma frequency at $y=\infty$ is $\sqrt{10}\omega_p$, and the thermal velocity at $y=\infty$ is $v_t/\sqrt{10}$ to satisfy the plasma pressure balance. Particles are loaded according to the shifted Maxwell distribution function with the drift velocity $u_0(y)$ and the thermal velocity $v_{ts}(y)$. The grid spacing is set as $\Delta=8.0v_{ti}/\omega_{pi}(=1.43r_i)$. Note that the electron Debye length is equal to the ion Debye length with these parameters, and that the grid spacing is set to be much longer than the electron/ion Debye length for $y \gg 0$ and is almost equal to the electron/ion Debye length for $y \ll 0$ in the present simulation. The simulation domain is taken from $x/l=0 \sim 11.2$ and $y/l=-7 \sim 7$. Thus the present simulation parameters are chosen so that the most unstable KH vortex grows at the maximum wavenumber ($k=2\pi/L_x \sim 0.56$). The periodic boundary condition is imposed in the x direction while open boundary condition is imposed in the y direction.

It should be note that the convective (motional) electric field is applied in the y direction,

$$E_y(y) = -\frac{B_0 u_0}{2}\tanh(y/l), \tag{19}$$

where $B_0 \equiv \omega_{ci} m_i/q_i$. In order to apply the self-consistent convective electric field, the electron number density is slightly modified such that Gauss's law is satisfied,[20]

$$n_e(y) = n_i(y) + \frac{\epsilon_0 B_0 u_0}{2 l q_i}\frac{1}{\cosh^2(y/l)}. \tag{20}$$

Therefore, the system is not charge neutral.

B. Simulation result

Figure 2 shows the growth rate of the KH vortex obtained by the linear analysis of the ideal MHD equations.[6] Panel (a) shows the growth rate as a function of the wavenumber in the flow direction. The "x" mark in panel (a) represents the growth rate of the most unstable KH vortex obtained by the Vlasov simulation. The wavenumber is normalized by $1/l$. The growth rate is normalized by l/u_0. Panel (b) shows the time development of the most unstable KH vortex. The ordinate shows the power of the y component of the perturbed ion velocity at the most unstable wavenumber ($k_x \sim 0.56$), obtained by the Fourier transformation and averaging over the y direction. The velocity is normalized by the initial velocity jump. As a reference, the growth rate obtained by the linear analysis of the ideal MHD equations is also shown.

The present simulation is initiated with a MHD equilibrium, instead of a Vlasov–Maxwell equilibrium. The present simulation result shows that the growth rate in the simulation ($\gamma \sim 0.081 u_0/l$) is slightly smaller than that obtained by the linear analysis of the ideal MHD equation ($\gamma \sim 0.088 u_0/l$). Since the half thickness of the shear layer is set to be much longer than the ion cyclotron radius ($l=8r_i$), the fluid equilibrium is well satisfied at the initial state.[20–22] However, the reason of the difference in the growth rate between the linear analysis of the ideal MHD equation and the Vlasov simulation is because the MHD equilibrium approaches to a Vlasov–Maxwell equilibrium in the time scale of several ion cyclotron periods, in which the spatial profile of ion density is slightly modified from that in the MHD equilibrium. The saturation level is in agreement with the previous PIC simulation.[6]

Figure 3 shows spatial profiles of the ion number density at different times. The position and time are normalized by l and l/u_0, respectively. A KH vortex appears at the most unstable wavenumber. During the first turning over motion of the KH instability, secondary instabilities grow at outer and inner edges of the vortex. One of the secondary instabilities is identified as the RT instability, which is driven by a gravity. The RT instability takes place only at the density interface where a centrifugal force of a KH vortex works as the effective gravity acceleration. That is, the RT instability transports dense fluids to a tenuous region when $\nabla n \cdot \vec{g} < 0$ (e.g., Ref. 6). Small vortices due to the secondary RT instability are found at the outer edge of the high-dense vortex in Fig. 3. On the other hand, the secondary KH instability is excited by the strong shear flows inside the normal vortex, when $\nabla n \cdot \vec{g} > 0$ (e.g., Ref. 23). Small fluctuations due to the secondary KH instability are found at the inner edge of the high-dense vortex at $(x/l, y/l, tl/u_0) \sim (5, 1, 69.67)$ and at $(x/l, y/l, tl/u_0) \sim (2, 0, 83.61)$ in Fig. 3. However, their intensity may not be so strong because velocity shear is not strong in the primary KH vortex, and they do not evolve into vortices. The wavelength of the secondary KH instability is estimated as $\sim 3l$, corresponding to a spatial scale of $1/4 \sim 1/5$ of the primary KH vortex, which is consistent with the previous two-fluid simulation.[7]

In Fig. 4, we show the cross sections of ion density at different times. At the initial state, the "full width" of the boundary layer from the high-dense region to the low-dense region is $>40r_i$ (the half thickness $l=8r_i$). A thin boundary layer appears when a KH vortex starts to roll up. From Fig. 4, we found that the full width of the boundary layer (between the local maximum and local minimum) is $\sim 8r_i = l$. We can estimate the half thickness of the boundary layer due to the primary KH vortex as $l_1 \sim 2r_i$. In the previous two-fluid simulation,[7] it has been found that the half thickness of boundary layer becomes 1/4 of the initial half thickness, which is consistent with the present Vlasov simulation result. As seen in Figs. 4(a)–4(d), this thickness ($l_1 \sim 0.25l$) is maintained constant during the nonlinear development of the KH instability, suggesting that the fluid approximation is well satisfied when the initial half thickness of a shear layer is much longer than the ion cyclotron radius. We also expand the cross section of the ion density profile around a secondary RT vortex at $(x/l, y/l, tl/u_0) \sim (2, -5, 83.61)$ in Fig. 3, which is shown in Fig. 4(e). We found that the full width of the boundary layer due to secondary vortices becomes $\sim r_i$. This result implies that the spatial scale of boundary layer due to secondary vortices is determined by the ion cyclotron radius in kinetic simulations, while the spatial scale of boundary layer becomes shorter and shorter as a fractal in fluid simulations. It should be noted, however, that the grid spacing of the present Vlasov simulation is close to the ion cyclotron radius, and that a higher-resolution simulation run would be necessary.

To identify the spatial scale of small vortices due to the secondary instability, we perform a Fourier analysis of the convection electric field. In Fig. 5, we show the spectrum of the E_x component at different times, which is obtained by Fourier transformation in both x and y directions and by averaging over the y direction. Figure 5 shows that the intensity of the spectrum becomes larger as the time elapses, but it saturates at $t \sim 70$. The power-law index becomes ~ -0.7 for $kr_i < 3$, and ~ -2.5 for $kr_i > 3$ after the saturation. That is, the power-law index changes at $kr_i \sim 3$, suggesting that the spatial scale of small vortices is determined by the ion cyclotron radius (e.g., Ref. 6). The saturation of spectral

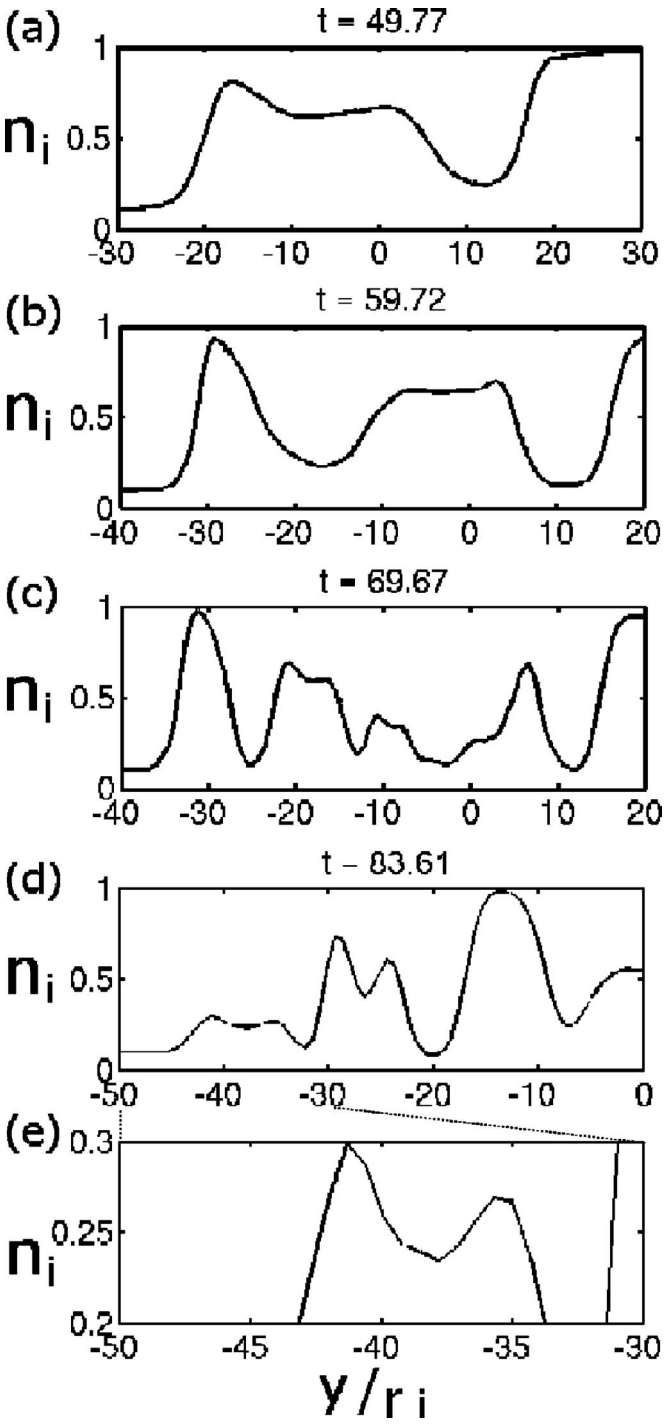

FIG. 4. The cross sections of ion density at different times: n_i at (a) $x/l=0$, (b) $x/l=10$, (c) $x/l=9$, and (d) $x/l=2$. (e) Expansion of panel (d) from $y/r_i=-50 \sim -30$. The position is normalized by the ion cyclotron radius r_i.

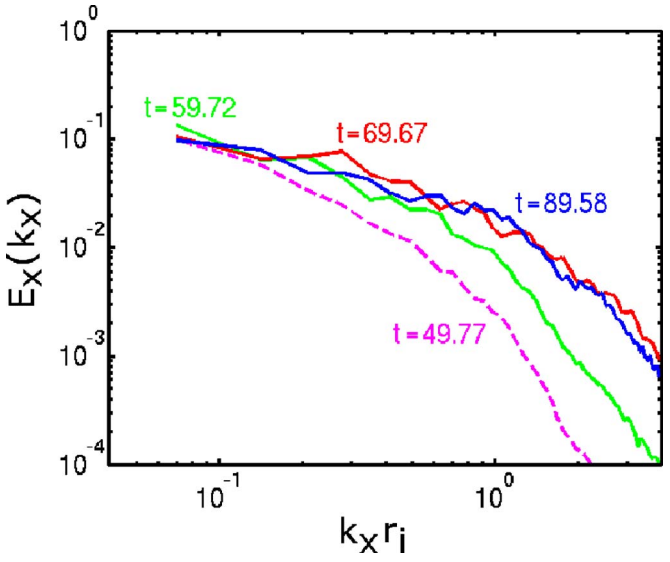

FIG. 5. (Color online) The spectrum of the E_x component at different times. The intensity is normalized by the convective electric field $B_0 u_0$. The wavenumber is normalized by the inverse of ion cyclotron radius $1/r_i$.

intensity for $kr_i > 3$ indicates that the energy cascade from the MHD-scale vortex to small-scale vortices is suppressed by the ion cyclotron motion.

C. Convergence test

We also changed the number of gird cells for the velocity space as $N_{v_x} \times N_{v_y} = 60 \times 60$ (run B) and 40×40 (run C). Figure 6 shows spatial profiles of the ion number density at different times with the same format as Fig. 3. Development of the KH instability in run B is consistent with run A. That is, the growth rate is almost the same in both runs, although the phase of the most unstable mode is slightly different. In run C, by contrast, the center of the KH vortex shifts in the $-y$ direction, suggesting that $N_{v_x} \times N_{v_y} = 40 \times 40$ is not enough for following the $\vec{E} \times \vec{B}$ drift. Numerical diffusion in the velocity space is an issue in the Vlasov method. The numerical diffusion is strong when the resolution in velocity space is low. In this case, the thermal pressure of plasma is numerically enhanced. In the present simulation model, there exists a high-dense and cold plasma for $y > 0$ and a low-dense and hot plasma for $y < 0$. Since the temperature is numerically enhanced in both regions, the plasma pressure becomes higher in the high-dense region. Thus the high-dense plasma shifts into the low-dense region.

D. Comparison with PIC simulation

For a direct comparison, a 2D full PIC simulation is also performed with the same physical parameters. Due to the numerical constraint on the spatial grid in the PIC method, the grid spacing is set to be the initial Debye length. (That is, $\Delta = v_{ti}/\omega_{pi}$ in the PIC simulation and $\Delta = 8v_{ti}/\omega_{pi}$ in the Vlasov simulations.) The number of particles per cell is set as 25 to match the memory usage between the PIC and Vlasov simulations (~5 Gbytes). (That is, particle data and distribution function data in a $8v_{ti}/\omega_{pi}$ square are

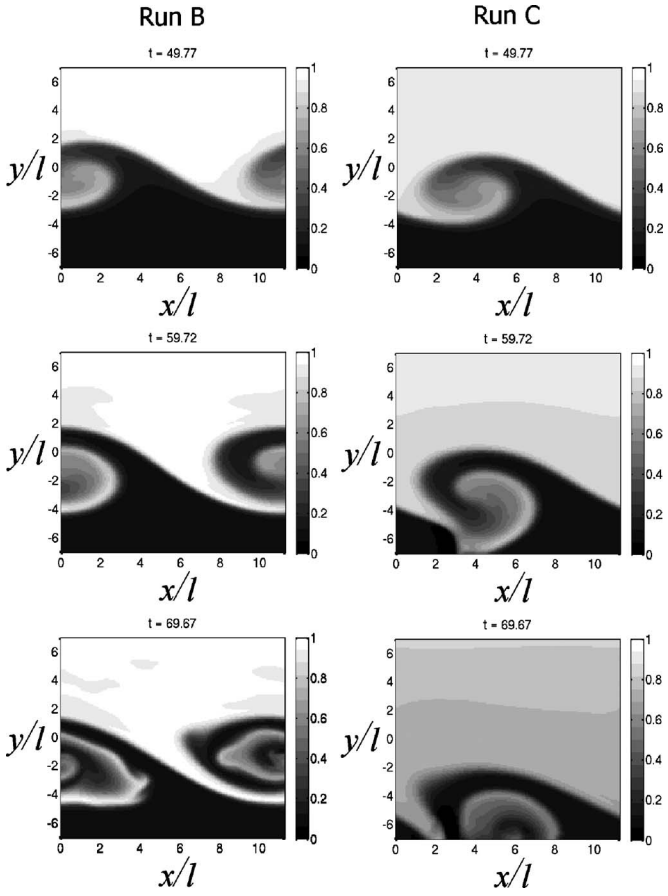

FIG. 6. Spatial profiles of the ion number density at different times in runs B and C. The time is normalized by l/u_0.

$8^2 \times 25 \times 4 (:x, y, v_x, v_y)$ and 80×80, respectively). For the entire computation, the PIC simulation took about 11 days on a quad-core 2.5 GHz Opteron processor, while the Vlasov simulation took about 45 days on the same processor. Thus the PIC code runs about four times faster than the Vlasov code *when the memory usage is almost the same*, suggesting that the computational cost of the Vlasov method is more expensive than that of the PIC method.

Figure 7 shows the result of direct comparison between Vlasov and PIC simulations at $t = 69.67$. The ion density distribution in Fig. 7(a) is obtained in the PIC simulation, which shows the existence of electron-scale small structures (also see Fig. 7 in Ref. 6). This is because of a higher spatial resolution in the PIC simulation than in the Vlasov simulation. In Figs. 7(b) and 7(c), we show ion velocity distribution functions around the center of the primary KH vortex in a $8v_{ti}/\omega_{pi}$ square obtained in the PIC and Vlasov simulations, respectively. There exist two components in both ion velocity distribution functions. One is majority cold population from the high-density region drifting in the $-x$ direction, and the other is minority nonthermal population from the low-density region. In the PIC simulation, the minority population is more scattered in the velocity space than in the Vlasov simulation, possibly because of the electron-scale small vortices or numerical thermal fluctuations.

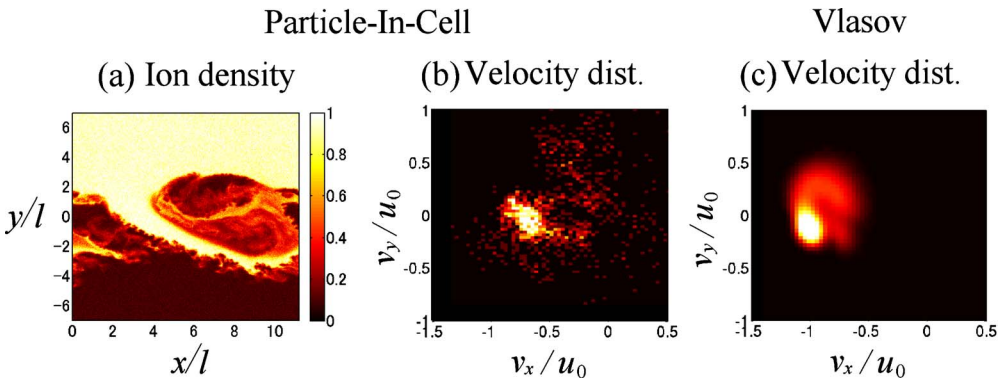

FIG. 7. (Color online) Direct comparison between Vlasov and PIC simulations. (a) Ion density distributions at $t=69.67$. (b) The ion velocity distribution function at $(x/l, y/l)=(9, -0.5)$ and $t=69.67$ in the PIC simulation. (c) The ion velocity distribution function at $(x/l, y/l)=(9, -1.5)$ and $t=69.67$ in the Vlasov simulation.

V. SUMMARY

A 4D (2D configuration and 2D velocity spaces) full electromagnetic Vlasov simulation of the KH instability is presented. Because of numerical difficulties, the KH instability is usually adopted as a benchmark test problem of guiding-center Vlasov codes. That is, there is no benchmark test of full electromagnetic Vlasov codes by the KH instability since it is difficult to follow $\vec{E}\times\vec{B}$ drift accurately on the Cartesian grid system. Thus the present study would be one of the first attempts to represent several processes taking place in the KH instability as obtained by previous PIC simulations (e.g., Ref. 6).

The combination of the modified splitting scheme[5,17] and the backsubstitution scheme[14] is useful for following the $\vec{E}\times\vec{B}$ drift even with a few number of grid cells for the velocity space. However, the method requires more than 60 grid cells for one velocity direction in order to suppress numerical diffusion of a velocity distribution function during the cyclotron motion.

In the present Vlasov simulation, the effect of the ion cyclotron motion for a MHD process has also been studied. We have observed that the boundary layer between high-dense and low-dense regions has two different spatial scales during the development of the KH instability. The half thickness of the boundary layer due to the primary KH vortex is maintained at 1/4 of the initial half thickness, which is consistent with the previous two-fluid simulation.[7] On the other hand, the thickness of the boundary layer due to secondary vortices becomes a spatial scale of ion cyclotron radius. The Fourier analysis has also shown that the power-law index of the convection electric field spectrum changes at $kr_i \sim 3$, implying that spatial scale of small vortices due to secondary RT and/or KH instabilities is determined by the ion cyclotron radius (e.g., Ref. 6). The present Vlasov simulation has successfully confirmed these cross-scale coupling processes between the MHD- and ion scales in the KH instability. However, due to the lack of spatial resolution, the effect of the electron cyclotron motion is not included in the present simulation, and hence high-resolution simulations are left as a future study.

In the present study, we assumed a simple geometry in which a uniform out-of-plain magnetic field exists without in-plain magnetic fields. In a more realistic case, however, in-plain magnetic fields can be strongly modified via cross-scale coupling (e.g., Ref. 8). For Vlasov simulations in the realistic geometry, we need to take the simulation domain in the five-dimensional (5D) phase space with two spatial dimensions and three velocity dimensions. Such a 5D full electromagnetic Vlasov simulation with a high spatial resolution requires a large computer memory of more than five terabytes. As shown in Sec. III, however, we have also successfully obtained a high performance in a weak-scaling test on a massively parallel computer with multicore scalar processors. In the recent days, computer hardware technologies are also rapidly developing. Although there are several numerical issues in the current Vlasov method, its numerical techniques are also rapidly developing. Thus it would be possible to include microscale physics in MHD-scale processes via full electromagnetic Vlasov simulations. In the near future, the Vlasov method would be a useful method for studies of cross-scale coupling in the plasma universe.

ACKNOWLEDGMENTS

This work was supported by the Grant-in-Aid for Young Scientists (B) No. 21740352 and in part by Grant-in-Aid for Creative Scientific Research No. 17GS0208 from MEXT of Japan. The computer simulations were performed on the Fujitsu FX1 supercomputer systems at the Information Technology Center in Nagoya University and Engineering Digital Innovation center in Japan Aerospace Exploration Agency (JAXA). The computational resource was provided by Solar-Terrestrial Environment Laboratory (STEL) in Nagoya University and Institute of Space and Astronautical Science (ISAS) in JAXA as a collaborative computational research project.

APPENDIX: MULTIDIMENSIONAL CONSERVATIVE SCHEME

Let us consider that a numerical solution to Eq. (8) takes the following conservative form:

$$f_s^*(x_i,y_j,v_{x,l},v_{y,m}) = f_s^t(x_i,y_j,v_{x,l},v_{y,m}) - \frac{\Delta t}{\Delta x}[U_{x,s}(x_{i+(1/2)},y_j,v_{x,l},v_{y,m}) - U_{x,s}(x_{i-(1/2)},y_j,v_{x,l},v_{y,m})] - \frac{\Delta t}{\Delta y}[U_{y,s}(x_i,y_{j+(1/2)},v_{x,l},v_{y,m}) - U_{y,s}(x_i,y_{j-(1/2)},v_{x,l},v_{y,m})], \quad \text{(A1)}$$

where U_x and U_y are numerical fluxes in the x and y directions, respectively. The subscripts i, j, l, and m represent the grid numbers. Then, the current-continuity equation (3) is automatically satisfied because the equation is obtained by integration (sum) of the above equation over the velocity space.

Although there is an arbitrary solution for the multidimensional numerical flux in Eq. (A1), we approximate the numerical flux by using a one-dimensional numerical flux U^{1D},

$$\left.\begin{aligned} U_{x,s}(x_{i+(\sigma_i/2)},y_j) &= U_{x,s}^{1D}(x_{i+(\sigma_i/2)},y_j)\left[1-\sigma_i\frac{\Delta t}{\Delta y}\frac{U_{y,s}^{1D}(x_i,y_{j+(\sigma_j/2)})}{2f_s^t(x_i,y_j)}\right] \\ U_{x,s}(x_{i+(\sigma_i/2)},y_{j+\sigma_j}) &= \sigma_i\frac{\Delta t}{\Delta y}\frac{U_{x,s}^{1D}(x_{i+(\sigma_i/2)},y_j)U_{y,s}^{1D}(x_i,y_{j+(\sigma_j/2)})}{2f_s^t(x_i,y_j)} \\ U_{y,s}(x_i,y_{j+(\sigma_j/2)}) &= U_{y,s}^{1D}(x_i,y_{j+(\sigma_j/2)})\left[1-\sigma_j\frac{\Delta t}{\Delta x}\frac{U_{x,s}^{1D}(x_{i+(\sigma_i/2)},y_j)}{2f_s^t(x_i,y_j)}\right] \\ U_{y,s}(x_{i+\sigma_i},y_{j+(\sigma_j/2)}) &= \sigma_j\frac{\Delta t}{\Delta x}\frac{U_{x,s}^{1D}(x_{i+(\sigma_i/2)},y_j)U_{y,s}^{1D}(x_i,y_{j+(\sigma_j/2)})}{2f_s^t(x_i,y_j)} \end{aligned}\right\} \quad \text{(A2)}$$

where $\sigma_i=\text{sign}(v_{x,l})$ and $\sigma_j=\text{sign}(v_{y,m})$. Note that $v_{x,l}$ and $v_{y,m}$ are omitted for simplicity. Here the one-dimensional numerical flux U^{1D} is computed by using a set of one-dimensional data. For an example, a numerical flux in the x direction, $U_x^{1D}(x_{i+(1/2)},y_j)$, is obtained as a function of $f(x_i,y_j)$, $f(x_{i-1},y_j)$, $f(x_{i+1},y_j)$, $f(x_{i-2},y_j)$, $f(x_{i+2},y_j)$,…. The detailed derivation is given in Ref. 5.

We can use an arbitrary conservative scheme to compute the one-dimensional numerical flux U^{1D}. In the present study, we use the positive, conservative, and nonoscillatory scheme.[13] Let us consider numerical solutions to the one-dimensional advection equation

$$\frac{\partial f}{\partial t} + v\frac{\partial f}{\partial x} = 0. \quad \text{(A3)}$$

The general solution of Eq. (A3) is obtained as

$$f(t+\Delta t, i\Delta x) = f(t, i\Delta x - v\Delta t) \quad \text{(A4)}$$

and a numerical solution with the third-order upwind-biased Lagrange polynomial interpolation is obtained as

$$f(x) = f_i + (x-i)(f_i - f_{i-1}) + (x-i)(1+x-i)(2+x-i)\frac{f_{i-1}-2f_i+f_{i+1}}{6} + (x-i)(1+x-i)(1-x+i)\frac{f_{i-2}-2f_{i-1}+f_i}{6}. \quad \text{(A5)}$$

The conservative form of the above equation is

$$U_{i+1/2}(\nu) = \nu f_i + \nu(1-\nu)(2-\nu)\frac{f_{i+1}-f_i}{6} + \nu(1-\nu)(1+\nu)\frac{f_i-f_{i-1}}{6}, \quad \text{(A6)}$$

where $\nu=i-x$ with

$$f_i^{t+\Delta t} = f_i^t + U_{i-(1/2)}(\nu) - U_{i+(1/2)}(\nu). \quad \text{(A7)}$$

We introduce a flux limiter in Eq. (A6) to suppress the numerical oscillation (e.g., Ref. 12),

$$U_{i+(1/2)}(\nu) = \nu f_i + \nu(1-\nu)(2-\nu)\frac{L_i^{(+)}}{6} + \nu(1-\nu)(1+\nu)\frac{L_i^{(-)}}{6}, \quad \text{(A8)}$$

where

$$L_i^{(+)} = \begin{cases} \min[2(f_i-f_{\min}),(f_{i+1}-f_i)] & \text{if} \quad f_{i+1}\geq f_i \\ \max[2(f_i-f_{\max}),(f_{i+1}-f_i)] & \text{if} \quad f_{i+1}<f_i, \end{cases}$$

$$L_i^{(-)} = \begin{cases} \min[2(f_{\max}-f_i),(f_i-f_{i-1})] & \text{if} \quad f_i\geq f_{i-1} \\ \max[2(f_{\min}-f_i),(f_i-f_{i-1})] & \text{if} \quad f_i<f_{i-1}, \end{cases}$$

with

$$f_{\max} = \max[f_{\max\,1}, f_{\max\,2}],$$

$$f_{\min} = \max[0, \min(f_{\min\,1}, f_{\min\,2})],$$

and

$$f_{\max 1} = \max[\max[f_{i-1}, f_i], \min[2f_{i-1} - f_{i-2}, 2f_i - f_{i+1}]],$$

$$f_{\max 2} = \max[\max[f_{i+1}, f_i], \min[2f_{i+1} - f_{i+2}, 2f_i - f_{i-1}]],$$

$$f_{\min 1} = \min[\min[f_{i-1}, f_i], \max[2f_{i-1} - f_{i-2}, 2f_i - f_{i+1}]],$$

$$f_{\min 2} = \min[\min[f_{i+1}, f_i], \max[2f_{i+1} - f_{i+2}, 2f_i - f_{i-1}]].$$

The detailed derivation is given in Ref. 13.

[1] P. Ricci, G. Lapenta, and J. U. Brackbill, J. Comput. Phys. **183**, 117 (2002).
[2] P. Ricci, G. Lapenta, and J. U. Brackbill, Geophys. Res. Lett. **29**, 2088, doi:10.1029/2002GL015314 (2002).
[3] J. Birn, J. F. Drake, M. A. Shay, B. N. Rogers, R. E. Denton, M. Hesse, M. Kuznetsova, Z. W. Ma, A. Bhattacharjee, A. Otto, and P. L. Pritchett, J. Geophys. Res. **106**, 3715, doi:10.1029/1999JA900449 (2001).
[4] H. Schmitz and R. Grauer, Phys. Plasmas **13**, 092309 (2006).
[5] T. Umeda, K. Togano, and T. Ogino, Comput. Phys. Commun. **180**, 365 (2009).
[6] Y. Matsumoto and M. Hoshino, J. Geophys. Res. **111**, A05213, doi:10.1029/2004JA010988 (2006).
[7] T. K. M. Nakamura, D. Hayashi, M. Fujimoto, and I. Shinohara, Phys. Rev. Lett. **92**, 145001 (2004).
[8] T. K. M. Nakamura, M. Fujimoto, and A. Otto, J. Geophys. Res. **113**, A09204, doi:10.1029/2007JA012803 (2008).
[9] C. Z. Cheng and G. Knorr, J. Comput. Phys. **22**, 330 (1976).
[10] C. Z. Cheng, J. Comput. Phys. **24**, 348 (1977).
[11] N. V. Elkina and J. Büchner, J. Comput. Phys. **213**, 862 (2006).
[12] F. Filbet, E. Sonnendrucker, and P. Bertrand, J. Comput. Phys. **172**, 166 (2001).
[13] T. Umeda, Earth, Planets Space **60**, 773 (2008).
[14] H. Schmitz and R. Grauer, Comput. Phys. Commun. **175**, 86 (2006).
[15] K. S. Yee, IEEE Trans. Antennas Propag. **AP-14**, 302 (1966).
[16] M. Hoshino, Ph.D. thesis, University of Tokyo, 1986.
[17] A. Ghizzo, F. Huot, and P. Bertrand, J. Comput. Phys. **186**, 47 (2003).
[18] S. J. Plimpton, D. B. Seidel, M. F. Pasik, R. S. Coats, and G. R. Montry, Comput. Phys. Commun. **152**, 227 (2003).
[19] E. Sonnendrücker, J. Roche, P. Bertrand, and A. Ghizzo, J. Comput. Phys. **149**, 201 (1999).
[20] P. L. Pritchett and F. V. Coroniti, J. Geophys. Res. **89**, 168, doi:10.1029/JA089iA01p00168 (1984).
[21] D. Cai, L. R. O. Storey, and T. Neubert, Phys. Fluids **2**, 75 (1990).
[22] D. Cai, L. R. O. Storey, and T. Neubert, J. Comput. Phys. **107**, 84 (1993).
[23] Y. Matsumoto and M. Hoshino, Geophys. Res. Lett. **31**, L02807, doi:10.1029/2003GL018195 (2004).